

Measurement-Based Fast Coordinated Voltage Control for Transmission Grids

Zhiyuan Tang, *Member, IEEE*, Etinosa Ekomwenrenren, *Student Member, IEEE*,
John W. Simpson-Porco, *Member, IEEE*, Evangelos Farantatos, *Senior Member, IEEE*,
Mahendra Patel, *Fellow, IEEE*, and Hossein Hooshyar, *Senior Member, IEEE*

Abstract—The increasing integration of utility-scale renewable energy sources (RESs) brings emerging challenges to the classical problems of voltage control in transmission grids, including increased potential for voltage violations. To address this challenge, we present a novel measurement-based coordinated voltage control scheme that can enable fast participation of RESs. In this approach, RESs are coordinated with the traditional voltage control devices such as synchronous generators (SGs) and static var compensators (SVCs) to maintain all bus voltages within operational limits while respecting device power limits. The control scheme allows different priorities to be assigned to different control resources, and ensures that both voltage and reactive power constraints are met in steady-state whenever it is possible to do so. The controller design requires only an approximate model of the steady-state relationships between voltage and reactive power in the system, and in online operation, processes voltage and reactive power measurements to produce set-point updates for RESs, SVCs, and SGs; this feedback provides robustness against both model uncertainty and unmeasured disturbances. The feasibility and effectiveness of the controller is demonstrated via simulation case studies on a detailed power system model.

Index Terms—Voltage control, measurement-based, transmission grid, renewable energy

I. INTRODUCTION

DRIVEN by environmental concerns, the penetration of utility-scale renewable energy sources (RESs) (e.g., wind/photovoltaic farms) is increasing in the transmission grid. The uncertainty and variability of RESs is putting increasing pressure on conventional voltage control strategies. These challenges include (but are not limited to) increased voltage fluctuations and violations, cascading tripping faults, and voltage stability issues such as fault-induced delayed voltage recovery (FIDVR) [1]–[3]. Advanced voltage control methods offer an appealing algorithmic solution to these challenges [1].

On the other hand, thanks to advances in power electronics, inverter-based RESs (IBRs) can be leveraged to provide fast reactive power support for voltage regulation if they are properly coordinated [4]. The key challenge becomes how

to coordinate IBRs with conventional voltage control devices such as synchronous generators (SGs) and static var compensators (SVCs) to provide fast and flexible voltage control services.

Traditionally, to schedule heterogeneous voltage control devices properly, an optimal reactive power flow (ORPF) problem is solved in control room operations [5] (e.g., the three-level hierarchical automatic voltage control in Europe [6] and adaptive zone-division-based automatic voltage control in China [7]). The optimal operation of control devices is calculated via frequently solving nonlinear, nonconvex ORPF problems, and the resulting set-points are sent to the control resources. Although powerful solvers and advanced optimization techniques have been designed specifically for this task (e.g., [8], [9]), such an offline optimization-based method requires a precise model of the physical power system and an accurate forecast of expected load and generation profiles [5], [10]. These models can be challenging to build and maintain in practice, and high penetration of RESs introduce increased uncertainty into the forecasting of load and generation. These robustness and forecasting issues can only be satisfactorily resolved by leveraging real-time or near-real-time measurements from the system and incorporating them into an *online* procedure for command scheduling.

Recently, the deployment of phasor measurement units (PMUs) and the development of wide-area measurement systems in transmission grids has opened the possibility of designing measurement-based voltage control schemes [11]–[13], where real-time measurements obtained from PMUs can be utilized for control purposes. A few measurement-based voltage control strategies have been proposed in the literature for transmission grids [14]–[16]. For example, in [14], a coordinated secondary voltage control scheme is proposed where PMU measurements are utilized to estimate reactive power load disturbances. Although voltage profiles in the system can be improved by the scheme, it lacks control flexibility, i.e. different priorities cannot be assigned by the system operator to different control resources. Moreover, the constraints involved in voltage controlling devices (e.g., SGs) only consider the voltage limits. Reactive power limits of these devices should also be considered since the control performance will be significantly influenced if these devices have reached their output limits. Furthermore, the method proposed in [14] is an offline algorithm. It is assumed in [14] that the load disturbance can be accurately estimated by the voltage deviation measurement obtained by PMUs,

Z. Tang and E. Ekomwenrenren are with the Department of Electrical and Computer Engineering, University of Waterloo, Waterloo, ON N3L 3G1 CA (e-mail: zhiyuan.tang@uwaterloo.ca; etinosa.ekomwenrenren@uwaterloo.ca).

J. W. Simpson-Porco is with the Department of Electrical and Computer Engineering, University of Toronto, 10 King's College Road, Toronto, ON, M5S 3G4, Canada (email: jwsimpson@ece.utoronto.ca).

E. Farantatos, M. Patel, and H. Hooshyar are with the Electric Power Research Institute, Palo Alto, CA 94304 USA (e-mail: efarantatos@epri.com; mpatel@epri.com; hhooshyar@epri.com).

This work was funded under EPRI Project #10009168: Wide-Area Hierarchical Frequency and Voltage Control for Next Generation Transmission Grids.

which is only satisfied when the system model is accurate and the system is in steady-state. System transients and model uncertainty may negatively impact this disturbance estimation, leading to performance degradation when implemented in real-time. In [16], based on model predictive control (MPC), a decentralized secondary voltage control scheme is developed where measured reactive power deviations on tie-lines between neighbouring areas are considered as measured disturbance by regional MPC controllers. Although MPC-based approaches have advantages of constraint satisfaction during transients, they are complex to implement, and an accurate dynamic power system model is required to compute the control actions. Such models can be challenging to obtain in practice, especially under high penetration of RESs.

Contributions: To address these issues, we develop and test a novel online voltage control strategy to quickly compensate unexpected voltage violations in the network using local resources. In the proposed method, IBRs and traditional voltage control equipment (SGs and SVCs) are coordinated to provide the fast and flexible voltage regulation. The control algorithm is designed based on the online approximate gradient method proposed in [10], which requires only a linearized and approximate relationship between the device set-points and the controlled variables (e.g., voltage and reactive power). A key feature of the proposed algorithm is the alternation between measurement and actuation based on the measured data, which can be considered as a feedback control strategy. While there have been several measurement-based (e.g. [17]–[20]) or feedback-based methods (e.g., [21]–[25]) proposed for voltage regulation in distribution networks, compared with all these works, the main contributions of this paper are:

- 1) To our best knowledge, we propose the first measurement-based online voltage control strategy for the *transmission* grid to handle unexpected voltage violations in real time. Compared with traditional offline optimization approaches (e.g. [14]), the proposed online algorithm has the advantages of improved robustness to model uncertainty and improved attenuation or rejection of unmeasured disturbances, which are illustrated in Scenarios 6 and 7 of Section III-A.
- 2) Given the dynamics of physical power system (*physical layer*) and the proposed voltage control strategy (*cyber layer*), a rigorous stability analysis is provided for the whole closed-loop (*cyber-physical*) system. This analysis provides guidance regarding controller tuning for stability (see Section II-D for details).
- 3) Two modifications are proposed for the designed voltage control strategy to improve the control performance under some specific conditions. The first is the “derivative term” introduced in Section II-E, which influences the transient response and leads to a two time-scale control framework. The second is the voltage recovery term designed in Section II-F, which ensures that voltages return to their pre-disturbance values after a three-phase fault.
- 4) Extensive case studies are conducted on the detailed power systems models in Section III to demonstrate the effectiveness and advantages of the proposed voltage control scheme, including the basic effectiveness test,

device limits violation test, different steady-state priorities test, model uncertainty test, time-delay test, measurement noise test, “derivative term” test, voltage recovery term test, FIDVR test, large sampling period test, one-area and multi-area test, and comparison with offline methods.

Organization: Section II introduces the details of the proposed voltage control strategy. Various case studies through full-order nonlinear power system models are given in Section III. Conclusions are presented in Section IV.

II. A MEASUREMENT-BASED COORDINATED VOLTAGE CONTROLLER FOR TRANSMISSION GRIDS

In this section, the details of the proposed online voltage control scheme will be introduced, including the overall control architecture, problem formulation, algorithm developments, stability analysis, and extensions. Our discussion in Sections II-A through II-F applies to a single control area within a transmission grid; the extension to the multi-area case is described in Section II-G.

A. High-Level Control Architecture

Our approach considers the transmission grid as a cyber-physical system, in which the *physical layer* consists of the transmission infrastructure (including transmission lines, SGs, loads, SVCs, and IBRs with their associated local controllers) and the *cyber layer* consists of wide-area measurement and communication infrastructure, along with the supervisory decision-making rules we will propose.

Our basic assumption is that the physical power system is stable, in the sense that when the system is subject to reasonable disturbances or changes in control set-points, a new stable operating point is quickly attained after transients; this will be made rigorous in Section II-D. Our supervisory voltage controller will operate in real-time with a specified sampling period, processing measurements from the system to produce updates to the set-points of devices. This results in a closed-loop power system where the physical and cyber layers are dynamically interconnected (see Fig. 1), and thus our approach is an area-wide feedback control strategy [5].

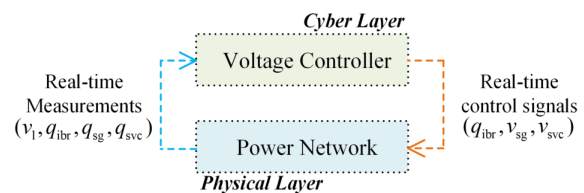


Figure 1: Cyber-physical system illustrating control approach.

B. ORPF Problem Formulation

The high-level control objective is to make efficient use of control resources (SGs, SVCs, and IBRs) in order to maintain bus voltages across the system within operational bounds. Our voltage controller will accomplish this by providing coordinated set-point updates to these devices subject to constraints

on their reactive power outputs. We let \mathbf{v}_{sg} and \mathbf{v}_{svc} denote the vectors of voltage *set-points* for SGs and SVCs respectively, with \mathbf{q}_{sg} and \mathbf{q}_{svc} denoting the vectors of resulting *steady-state* reactive power outputs. We assume that IBRs are equipped with local power tracking control loops, and hence accept power set-points, with \mathbf{q}_{ibr} denoting the vector of IBR reactive power set-points. We collect all device set-points into a stacked vector $\mathbf{u} = \text{col}(\mathbf{q}_{\text{ibr}}, \mathbf{v}_{\text{sg}}, \mathbf{v}_{\text{svc}})$, and let

$$\mathcal{U} := [\underline{\mathbf{q}}_{\text{ibr}}, \bar{\mathbf{q}}_{\text{ibr}}] \times [\underline{\mathbf{v}}_{\text{sg}}, \bar{\mathbf{v}}_{\text{sg}}] \times [\underline{\mathbf{v}}_{\text{svc}}, \bar{\mathbf{v}}_{\text{svc}}] \quad (1)$$

denote the set of upper and lower limits associated with these set-point commands. The control effort provided by these devices will be quantified by a quadratic function penalizing the deviation of the device reactive power outputs from their dispatch points \mathbf{q}_{sg}^* , $\mathbf{q}_{\text{svc}}^*$, $\mathbf{q}_{\text{ibr}}^*$ written as

$$f(\mathbf{q}_{\text{ibr}}, \mathbf{q}_{\text{sg}}, \mathbf{q}_{\text{svc}}) = (\Delta \mathbf{q}_{\text{ibr}})^\top \mathbf{R}_{\text{ibr}} (\Delta \mathbf{q}_{\text{ibr}}) + (\Delta \mathbf{q}_{\text{sg}})^\top \mathbf{R}_{\text{sg}} (\Delta \mathbf{q}_{\text{sg}}) + (\Delta \mathbf{q}_{\text{svc}})^\top \mathbf{R}_{\text{svc}} (\Delta \mathbf{q}_{\text{svc}}) \quad (2)$$

where $\Delta \mathbf{z} = \mathbf{z} - \mathbf{z}^*$ denotes deviation and \mathbf{R}_{ibr} , \mathbf{R}_{sg} , $\mathbf{R}_{\text{svc}} \succ 0$ are positive definite diagonal matrices. Tuning of \mathbf{R}_{ibr} , \mathbf{R}_{sg} , \mathbf{R}_{svc} allows for the designer to adjust which devices contribute more or less power in steady-state; this will be illustrated in Section III, Scenario 3.

Let \mathbf{v}_1 denote the vector of bus voltage magnitudes at all *load* buses, which for our purposes are the system buses which are not voltage-regulated (i.e., not attached to an SG or SVC). These voltages are subject to operational limits $\underline{\mathbf{v}}_1 \leq \mathbf{v}_1 \leq \bar{\mathbf{v}}_1$. In a standard offline ORPF, the optimal set-points for the control devices are computed to minimize (2) subject to voltage constraints at all load buses and subject to device reactive power constraints as

$$\underset{\mathbf{u} \in \mathcal{U}}{\text{minimize}} \quad f(\mathbf{q}_{\text{ibr}}, \mathbf{q}_{\text{sg}}, \mathbf{q}_{\text{svc}}) \quad (3a)$$

$$\text{s.t.} \quad (\mathbf{q}_{\text{ibr}}, \mathbf{q}_t, \mathbf{v}_1) = \pi_{\text{ps}}(\mathbf{u}, \mathbf{w}) \quad (3b)$$

$$\underline{\mathbf{v}}_1 \leq \mathbf{v}_1 \leq \bar{\mathbf{v}}_1 \quad (3c)$$

$$\underline{\mathbf{q}}_t \leq \mathbf{q}_t \leq \bar{\mathbf{q}}_t \quad (3d)$$

where $\mathbf{q}_t = \text{col}(\mathbf{q}_{\text{sg}}, \mathbf{q}_{\text{svc}})$ denotes the stacked vector of reactive power outputs for *traditional* resources, with operational limits defined in (3d). The disturbance \mathbf{w} in (3b) would usually model load and uncontrolled generation changes. The nonlinear function π_{ps} (3b) is the *steady-state* power flow model of the grid, which provides the relationship between inputs (device set-points \mathbf{u} and disturbances \mathbf{w}) and measurements $(\mathbf{q}_{\text{ibr}}, \mathbf{q}_t, \mathbf{v}_1)$.

An accurate solution of (3) is quite difficult in practice, as the grid model π_{ps} may be imperfectly known, and the disturbances \mathbf{w} must be replaced by the best available forecast $\hat{\mathbf{w}}$. This results in a lack of robustness to real-time operating changes, leading to voltage violations and inefficient use of control resources. Additionally, the hard constraints (3b) may be infeasible in practice due to insufficient reactive power control resources. We now develop an alternative online approach which will approximately solve (3) in real-time, leading to improved performance and robustness.

C. Online Algorithm for ORPF Solution

To begin addressing the issues mentioned above, we replace the hard inequality constraints (3c)–(3d) in (3) with *penalty functions*. For a vector $\mathbf{z} \in \mathbb{R}^n$ with limits $\underline{\mathbf{z}} \leq \mathbf{z} \leq \bar{\mathbf{z}}$ and a constant $a > 0$, define the penalty function

$$h_a(\mathbf{z}) = a \sum_{i=1}^n \max(0, \underline{z}_i - z_i, z_i - \bar{z}_i)^2. \quad (4)$$

This function is zero if $\underline{\mathbf{z}} \leq \mathbf{z} \leq \bar{\mathbf{z}}$, and grows quadratically if any component of \mathbf{z} violates the constraint. Using this in place of (3c)–(3d) yields the modified problem

$$\underset{\mathbf{u} \in \mathcal{U}}{\text{minimize}} \quad f(\mathbf{q}) + h_a(\mathbf{v}_1) + h_b(\mathbf{q}_t) \quad (5a)$$

$$\text{s.t.} \quad (\mathbf{q}, \mathbf{v}_1) = \pi_{\text{ps}}(\mathbf{u}, \mathbf{w}), \quad (5b)$$

where $\mathbf{q} = \text{col}(\mathbf{q}_{\text{ibr}}, \mathbf{q}_t)$ and $a, b > 0$ are penalty parameters. Large values of a, b will encourage the optimization problem to maintain the constraints, while not rigidly enforcing feasibility of (3c), which would be problematic in practice as explained above. While rigorous satisfaction of (3c) will not be guaranteed, small violations are perfectly tolerable in practical systems. As for the replacement of hard reactive power constraints (3d) in (3) with a penalty function, we note that this will not lead to unit reactive power violations in practice, as the outputs of SGs and SVCs are physically limited by saturation protection in the internal controllers. The penalty function however is much more convenient for the design of an online algorithm, which we are now ready to outline.

Based on recent feedback-based gradient methods [10], we propose using the following iteration as an online controller to solve (5):

$$\mathbf{u}^{k+1} = \text{Proj}_{\mathcal{U}}(\mathbf{u}^k - \tau \mathbf{F}(\mathbf{q}^k, \mathbf{v}_1^k)) \quad (6)$$

where $k \in \{0, 1, 2, \dots\}$ is the sampling time index, $\text{Proj}_{\mathcal{U}}(\xi)$ denotes the Euclidean projection of the vector ξ onto the set \mathcal{U} from (1), and $\tau > 0$ is a controller gain (step size). The values $(\mathbf{q}^k, \mathbf{v}_1^k)$ are the reactive power and bus voltage *measurements* taken from the system at sampling instant k , and the function \mathbf{F} is defined by

$$\mathbf{F}(\mathbf{q}, \mathbf{v}_1) = \mathbf{\Pi}_1^\top \nabla f(\mathbf{q}) + \mathbf{\Pi}_2^\top \nabla h_a(\mathbf{v}_1) + \mathbf{\Pi}_3^\top \nabla h_b(\mathbf{q}_t). \quad (7)$$

Here, ∇f , ∇h_a , and ∇h_b denote the gradients of the objective function components from (5). The matrices $\mathbf{\Pi}_1, \mathbf{\Pi}_2, \mathbf{\Pi}_3$ are *approximations* of the sensitivity Jacobian matrices $\frac{\partial \mathbf{q}}{\partial \mathbf{u}}$, $\frac{\partial \mathbf{v}_1}{\partial \mathbf{u}}$, and $\frac{\partial \mathbf{q}_t}{\partial \mathbf{u}}$ associated with the power flow mapping π_{ps} in (5). The expressions of $\mathbf{\Pi}_1, \mathbf{\Pi}_2$, and $\mathbf{\Pi}_3$ are given as follows:

$$\mathbf{\Pi}_1 = \begin{bmatrix} \frac{\partial \mathbf{q}_{\text{ibr}}}{\partial \mathbf{q}_{\text{ibr}}} & \frac{\partial \mathbf{q}_{\text{ibr}}}{\partial \mathbf{v}_t} \\ \frac{\partial \mathbf{q}_t}{\partial \mathbf{q}_{\text{ibr}}} & \frac{\partial \mathbf{q}_t}{\partial \mathbf{v}_t} \end{bmatrix}, \quad \mathbf{\Pi}_2 = \begin{bmatrix} \frac{\partial \mathbf{v}_1}{\partial \mathbf{q}_{\text{ibr}}} & \frac{\partial \mathbf{v}_1}{\partial \mathbf{v}_t} \end{bmatrix} \quad (8)$$

$$\mathbf{\Pi}_3 = \begin{bmatrix} \frac{\partial \mathbf{q}_t}{\partial \mathbf{q}_{\text{ibr}}} & \frac{\partial \mathbf{q}_t}{\partial \mathbf{v}_t} \end{bmatrix},$$

where $\mathbf{v}_t = \text{col}(\mathbf{v}_{\text{sg}}, \mathbf{v}_{\text{svc}})$ and all partial derivatives are evaluated at the underlying dispatch point.¹ The reasons for using the approximate Jacobian matrices $\mathbf{\Pi}$ in place of the *exact* partial derivative $\partial \pi_{\text{ps}} / \partial \mathbf{u}$ are as follows:

¹In our experiments, we have found essentially no difference in closed-loop performance if one instead evaluates at open-circuit conditions.

- (i) the system model π_{ps} may be difficult to accurately obtain, as it depends on both the transmission network data and on tunings of local (i.e., AVR) voltage controllers. In contrast, approximate sensitivity information is often known from experience and/or easily estimated;
- (ii) the partial derivative $\partial\pi_{\text{ps}}/\partial\mathbf{u}$ will in general depend on both \mathbf{u} and \mathbf{w} , the latter of which is unmeasured, and hence the exact sensitivity cannot be evaluated online;
- (iii) since (6)–(7) is a feedback law, the closed-loop system will naturally possess insensitivity to modelling uncertainty; the matrices $\mathbf{\Pi}$ are our approximate model of how the grid will respond, and this is all that is required for successful feedback design.

Given the above, it is sufficient to compute the matrices $\mathbf{\Pi}$ assuming that the power system is in steady-state, in which case the partial derivatives can be directly evaluated based on the network bus admittance matrix and the dispatch point; further details are given in Appendix A.

The iteration (6)–(7) acts as a feedback controller, producing the next control input \mathbf{u}^{k+1} as a function of the previous control input \mathbf{u}^k and the real-time measurements. The calculations needed to evaluate (6)–(7) are almost trivial; (7) is simple function evaluations with several matrix-vector multiplications, and the projection in (6) simply restricts the control signals to be within their upper and lower limits.

Remark II.1 (Comments on Gradient Algorithm). *The proposed controller (6)–(7) is inspired by the standard gradient descent method, which is known to converge slowly compared to other optimization algorithms. Here however, the situation and performance criteria are quite different than in a standard optimization setup. First, we use (6)–(7) as a supervisory feedback controller for a dynamic power system. Unlike standard static optimization problems, here we must focus on closed-loop stability, and we provide a closed-loop stability assessment in Theorem II.2. Second, although the gradient method is slow in terms of number of iterations to convergence, our controller runs with a fast sampling rate, allowing many iterations within a short period of time. As load and generation patterns persist over many minutes [26], we see that even with a low sampling rate, the control performance is still satisfactory within a short time period, which is demonstrated through Scenario 10 in Section III-A. Third, the proposed algorithm does not need to converge to its optimal solutions, since the proposed control strategy is designed for online application and needs to adapt to new disturbances in real time. As a final advantage, pure gradient methods are simple to implement and are known to be robust to noise compared to accelerated methods [27].*

D. Basic Insights on Tuning and Stability Theorem

The control scheme (6)–(7) contains several parameters which must be set; the feedback gain τ , the sensitivity matrices $\mathbf{\Pi}$, and the weights \mathbf{R} , a , and b contained in the objective functions. As mentioned previously, $\mathbf{\Pi}$ will be set based on a small-signal steady-state grid model and/or experience, and \mathbf{R} is set based on how the designer wishes to allocate steady-state

reactive power across different devices. Our experience is that a, b can be initially set at large values (e.g., 10^4), and increased further if constraint violation occurs due to contingencies of interest. Tuning of (6)–(7) then reduces to tuning the single parameter τ , which acts as an integral gain.

Our main theoretical result supporting the controller is that under reasonable technical assumptions, one can always select τ sufficiently small to ensure closed-loop stability. This allows for practical and classical tuning methods to be applied (e.g., [28]), where τ is set at a small value (e.g., $\frac{1}{10} \max\{a, b\}$) and then increased until acceptable performance is obtained. Assume that the *dynamic* power system is described at the *sampling instants* by a nonlinear discrete-time model

$$\begin{aligned} \mathbf{x}^{k+1} &= \mathbf{f}(\mathbf{x}^k, \mathbf{u}^k, \mathbf{w}) \\ (\mathbf{q}^k, \mathbf{v}_1^k) &= \mathbf{h}(\mathbf{x}^k, \mathbf{u}^k, \mathbf{w}) \end{aligned} \quad (9)$$

where \mathbf{x} is the state vector of the system. We *do not* require knowledge of the model (9), only that it satisfies the following mild technical assumptions:

- (A1) \mathbf{f} is continuously differentiable in all arguments on some closed convex set $\mathcal{X} \times \mathcal{V} \times \mathcal{W}$ contained in the normal system operating region, and \mathbf{f} , \mathbf{h} , $\frac{\partial \mathbf{f}}{\partial \mathbf{x}}$, $\frac{\partial \mathbf{f}}{\partial \mathbf{u}}$, and $\frac{\partial \mathbf{f}}{\partial \mathbf{w}}$ are all Lipschitz continuous in \mathbf{x} , uniformly in the inputs (\mathbf{u}, \mathbf{w}) ;
- (A2) for every constant $(\mathbf{u}, \mathbf{w}) \in \mathcal{V} \times \mathcal{W}$, the system (9) possess a unique equilibrium point $\pi_{\mathbf{x}}(\mathbf{u}, \mathbf{w}) \in \mathcal{X}$, and the function $\pi_{\mathbf{x}}$ is continuously differentiable and Lipschitz continuous on $\mathcal{V} \times \mathcal{W}$;
- (A3) the equilibrium $\pi_{\mathbf{x}}(\mathbf{u}, \mathbf{w})$ is locally exponentially stable, uniformly in $(\mathbf{u}, \mathbf{w}) \in \mathcal{V} \times \mathcal{W}$.

These conditions mathematically capture the idea that the power system is well-behaved, and converges to a unique equilibrium when reasonable constant inputs are applied. With the above notation, the steady-state power system model π_{ps} in (5) is in fact given exactly by $\pi_{\text{ps}}(\mathbf{u}, \mathbf{w}) = \mathbf{h}(\pi_{\mathbf{x}}(\mathbf{u}, \mathbf{w}), \mathbf{u}, \mathbf{w})$. Our final technical assumption is

- (A4) the composition $\mathbf{F} \circ \pi_{\text{ps}}$ maps $\mathcal{V} \times \mathcal{W}$ to \mathcal{V} and is *strongly monotone* in \mathbf{u} uniformly in \mathbf{w} .

Roughly speaking, (A4) means that $\mathbf{F} \circ \pi_{\text{ps}}$ is a strictly increasing function of the set-points \mathbf{u} . While we do not pursue further technical details here, we remark that (i) this is a standard condition for convergence of discrete iterations such as (6), (ii) the condition will automatically hold if π_{ps} is described with a linear model using the sensitivity matrices in (8), and (iii) a computational framework for verifying this condition for nonlinear power system models is available in [10]. Our experience is that this condition holds across all practical system operating points, as long as egregious errors are not made in selecting the sensitivity matrices (8).

We can now state the main stability theorem; for technical reasons pertaining to the proof (see Appendix B), the theorem is restricted to the case of (6) without the projection operation.

Theorem II.2 (Closed-Loop Stability with Measurement-Based Coordinated Voltage Control). *For the power system (9) with the voltage controller (6)–(7) under the previously mentioned assumptions, the closed-loop system possesses a*

as different in a particular scenario to follow. We additionally note that the scenarios considered are generally quite severe, in order to more clearly illustrate the action of the controller.

Table I: Parameter settings.

Quantity	Value	Comment
$[\underline{v}_l, \bar{v}_l]$	[0.95, 1.05] p.u.	Volatage limits of load buses
$[\underline{v}_{sg}, \bar{v}_{sg}]$	[0.95, 1.05] p.u.	Volatage set-point limits for SGs
$[\underline{v}_{svc}, \bar{v}_{svc}]$	[0.95, 1.05] p.u.	Volatage set-point limits for SVCs
$[\underline{q}_{ibr}, \bar{q}_{ibr}]$	[-1.2, 1.2] p.u.	Reactive output limits for IBRs
$[\underline{q}_{sg}, \bar{q}_{sg}]$	[-1.0, 1.0] p.u.	Reactive output limits for SGs
$[\underline{q}_{svc}, \bar{q}_{svc}]$	[-2.0, 2.0] p.u.	Reactive output limits for SVCs
\mathbf{R}_{ibr}	$100\mathbf{I}$	Weight matrix for IBRs in (2)
\mathbf{R}_{svc}	$100\mathbf{I}$	Weight matrix for SVCs in (2)
\mathbf{R}_{sg}	\mathbf{I}	Weight matrix for SGs in (2)
a	10^5	Penalty parameter in (5a)
b	10^3	Penalty parameter in (5a)
τ	10^{-5}	Step size
T_s	0.01 s	Sampling period

1) *Scenario 1 – Basic effectiveness test:* A 120 MVar reactive power disturbance occurs at bus 8 at $t = 5$ s. Fig. 3 shows the voltage and reactive power profiles during the disturbance. From Fig. 3, we see (in particular, at bus 8) that the controller responds immediately when a voltage violation is detected and regulates the voltage to within operational limits.

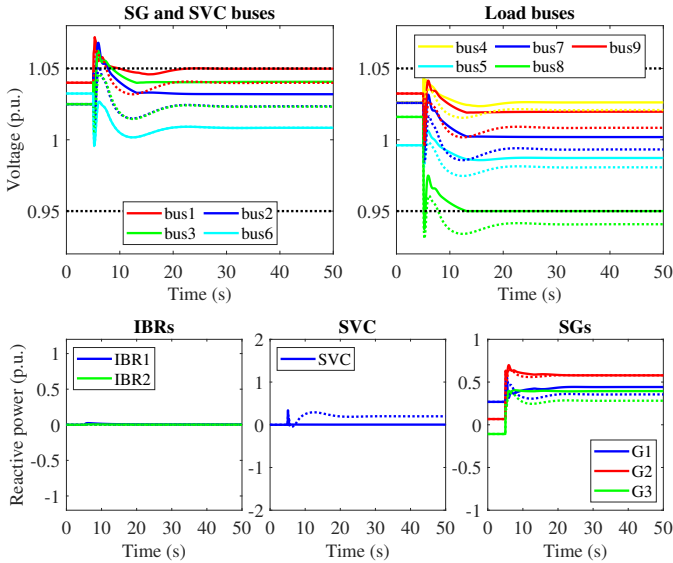


Figure 3: Voltage and reactive power profiles during disturbance in Scenario 1 (dotted: without control, solid: with control)

2) *Scenario 2 – Device output limits violation test:* We apply 120 and 75 MVar reactive power disturbances at buses 8 and 7 at $t = 5$ s, respectively, which tests the control performance when the reactive power output limits of devices are reached. To improve constraint satisfaction for this large disturbance, we increase the penalty parameters to $a = 10^{5.5}$ and $b = 10^4$, and accordingly decrease the step size to $\tau = 10^{-6}$. Fig. 4 shows the voltage and reactive power profiles during the disturbance. We observe that the reactive power outputs of devices (in particular, SG 2) are maintained

within limits, and bus voltage regulation (e.g., at bus 8) is substantially improved compared to without the controller.

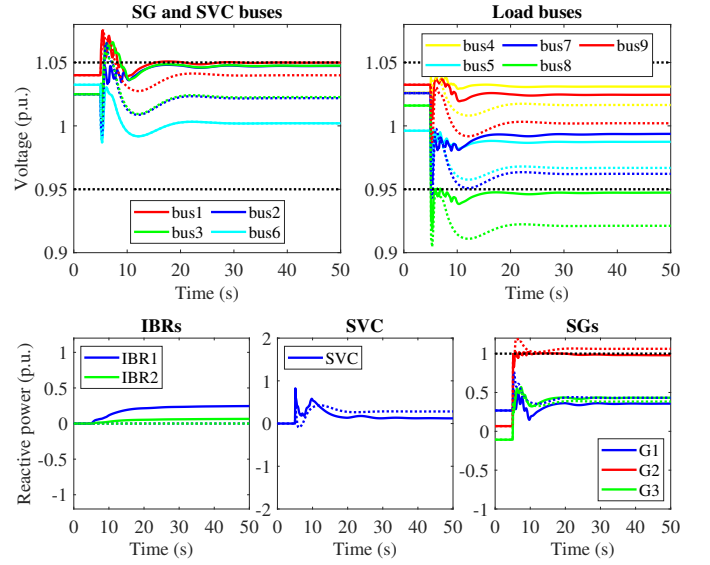


Figure 4: Voltage and reactive power profiles during disturbance in Scenario 2 (dotted: without control, solid: with control)

3) *Scenario 3 – Modifying the steady-state control priority:* We now modify the weighting matrices \mathbf{R} in (2) to prioritize different control resources; the disturbance is the same as in Scenario 1. Fig. 5 shows the voltage and reactive power profiles during disturbance, where the various line types correspond to the following prioritizations

- dotted line: $\text{SG} \gg \text{IBR} = \text{SVC}$
- solid line: $\text{IBR} = \text{SVC} \gg \text{SG}$
- dashed line: $\text{IBR} \gg \text{SG} = \text{SVC}$.

We observe that the weights in the proposed algorithm can be adjusted to change how aggressively different resources react to disturbances, and can be adjusted to allocate power across different devices as desired while still maintaining voltage and power limits for all devices.

4) *Scenario 4 – Improving the transient performance:* We now test the addition of the transient performance term described in Section II-E; the disturbance is the same as in Scenario 1. Here, we set $\tau_d = 20$. Fig. 6 shows the controlled voltage and reactive power profiles during disturbance. We observe that voltage violations are handled effectively by the proposed controller with different transient terms. From Fig. 6, we also see that (i) IBRs and SVCs contribute strongly during the transient control period, (ii) the transient response of IBRs and SVCs can be adjusted by changing the tuning matrix $\mathbf{\Pi}_d$, and (iii) the transient terms will vanish in steady state.

5) *Scenario 5 – Controller behaviour during FIDVR:* To produce a fault-induced delayed voltage recovery phenomena, the load at bus 5 is replaced with a large residential induction motor, whose parameters can be found in [31]. We apply a three-phase fault at $t = 0.1$ s at bus 5, and clear the fault at $t = 0.3$ s. Fig. 7 shows the short-term voltage profile during disturbance. From Fig. 7, we can see that the proposed approach can shorten the time period of FIDVR and the

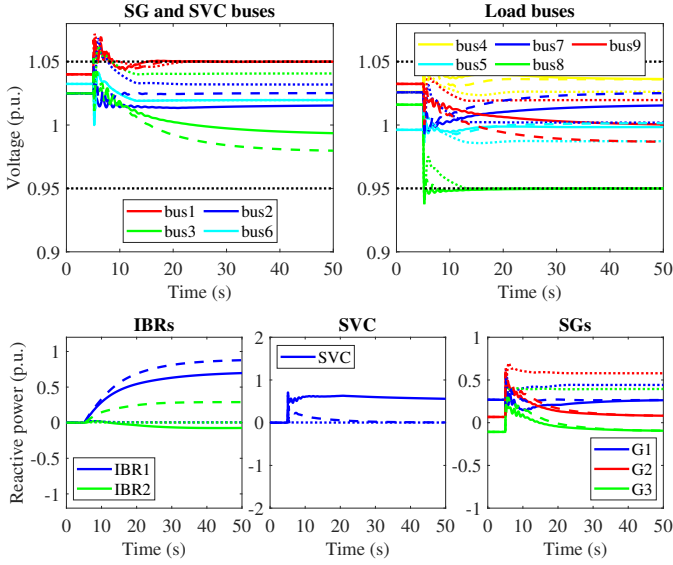


Figure 5: Voltage and reactive power profiles during disturbance in Scenario 3 (dotted: $R_{ibr} = R_{svc} = 100I$, $R_{sg} = I$, solid: $R_{ibr} = R_{svc} = I$, $R_{sg} = 100I$, dashed: $R_{sg} = R_{svc} = 100I$, $R_{ibr} = I$)

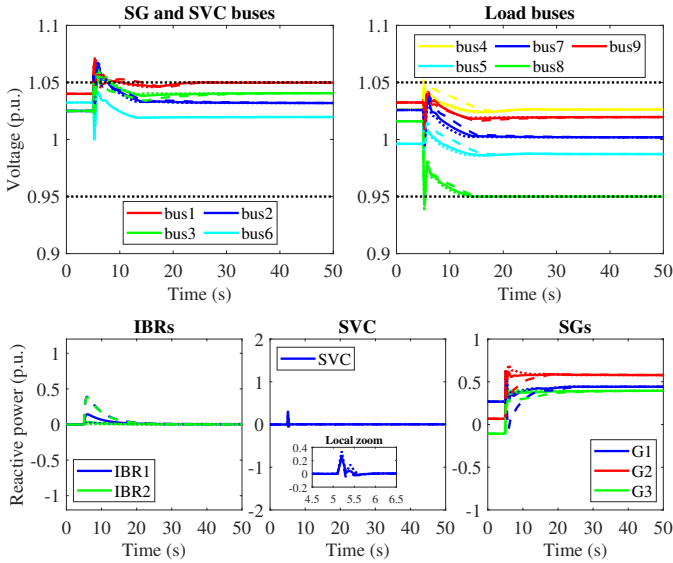


Figure 6: Voltage and reactive power profiles during disturbance in Scenario 4 (dotted: no transient term, solid: with gain matrix $\Pi_{d,1}$, dashed: with gain matrix $\Pi_{d,2}$).

duration of the event in this case is approximately one-half of the duration without control. Fig. 8 shows long-term voltage and reactive power profiles during disturbance. From Fig. 8, we see that, with the proposed controller voltages come back to the acceptable limits faster.

6) Scenario 6 – Comparison with an offline approach:

We compare the control performance of the proposed online scheme with that of an offline model-based ORPF; the disturbance is the same as in Scenario 1. In the offline approach, the optimal control actions are obtained by following the procedure in [14]. We first estimate the *steady-state* load

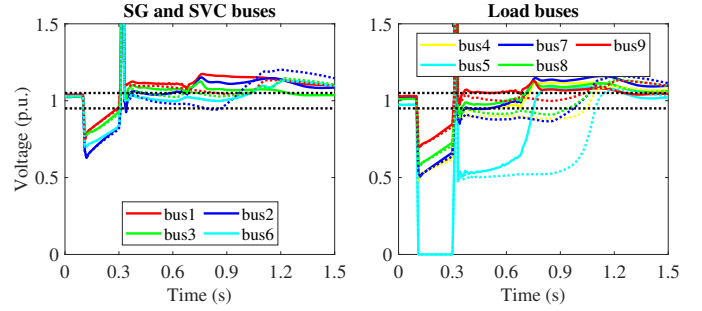


Figure 7: Short-term voltage profile during disturbance (dotted: without control, solid: with control)

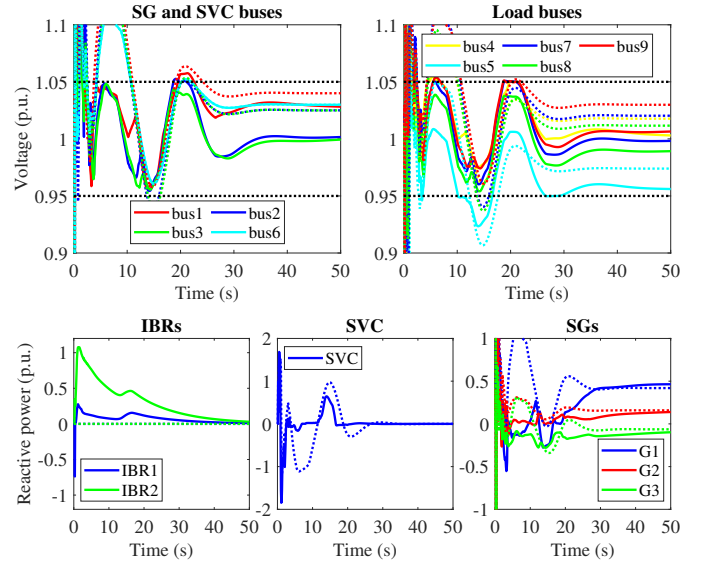


Figure 8: Long-term voltage and reactive power profiles during disturbance (dotted: without control, solid: with control)

disturbance value based on the perfect system information that includes the load type (impedance), initial disturbance value (120 MVar), and the steady-state load bus voltage magnitude after the disturbance (i.e., the voltage magnitude of bus 8 at $t = 50s$ with no control in Scenario 1). The estimated value of steady-state load disturbance is 106.21 MVar. Then, given this estimated steady-state disturbance value, the optimal control actions are calculated by solving the same voltage control problem (3) considered in the online algorithm with the same system model (i.e., (3b) is represented by (13)) and parameters. These control actions are implemented at the same time when the disturbance occurs. We note that this accurate estimated disturbance value would be very difficult to obtain in real implementation, and hence, our comparison will be charitable to the offline approach.

Fig. 9 shows the voltage and reactive power profiles during disturbance. The achieved steady-state objective function values of the proposed online approach and offline approach are 0.55 and 1.88, respectively. We observe that the proposed online algorithm can obtain almost the same solutions as the offline algorithm, but without the knowledge of perfect disturbance information which must be used in offline approach.

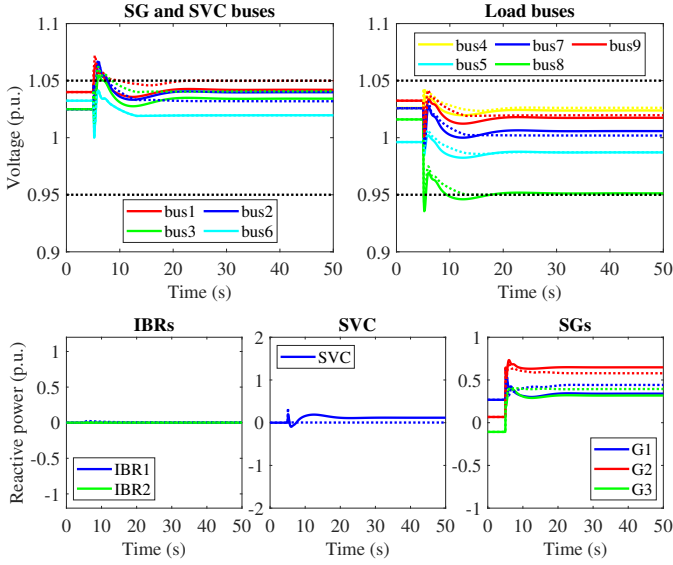


Figure 9: Voltage and reactive power profiles during disturbance in Scenario 6 (dotted: online, solid: offline)

7) *Scenario 7 – Model uncertainty test:* We now test the control performance when the approximate sensitivity information used in (5) is inaccurate due to the system topology reconfiguration, i.e., when significant model mismatch occurs. To this end, we apply 40 MVar reactive power disturbance at bus 8 at $t = 5$ s and trip the transmission line between buses 7 and 8 at the same time. Here, we consider three cases: one is obtained by the offline approach used in Scenario 6 with inaccurate sensitivity information, the other two are obtained by the proposed online approach with inaccurate and accurate sensitivity information, respectively, where the inaccurate sensitivity information is calculated based on the pre-line-trip system topology. Fig. 10 shows the voltage and reactive power profiles during disturbance. We observe that the proposed online approach can achieve good performance even with an inaccurate sensitivity model, while the offline method struggles to regulate voltages; the online method is robust to model uncertainty. Next, we compare the performances obtained by online approach with inaccurate and accurate sensitivity information. Recall that in this test, a line trip drastically changes the topology of the system, and hence, changes the sensitivity matrices which should be used in the control algorithm. The controller does indeed respond differently when sensitivity matrices are changed, and the performance is improved if the sensitivity matrix is accurate. A small persistent upper voltage violation occurs at load bus 7 when the sensitivity matrices are inaccurate. There are two reasons for this: 1) the controller is using incorrect sensitivity information, and believes that control actions at G2 and IBR1 will be more effective than they really are; and 2) voltage set-points of SGs have reached their upper limits.

8) *Scenario 8 – Communication delay test:* We now test the control performance when communication delay occurs in the proposed online controller, on *both* the measurements and the dispatch of set-points; the disturbance is the same

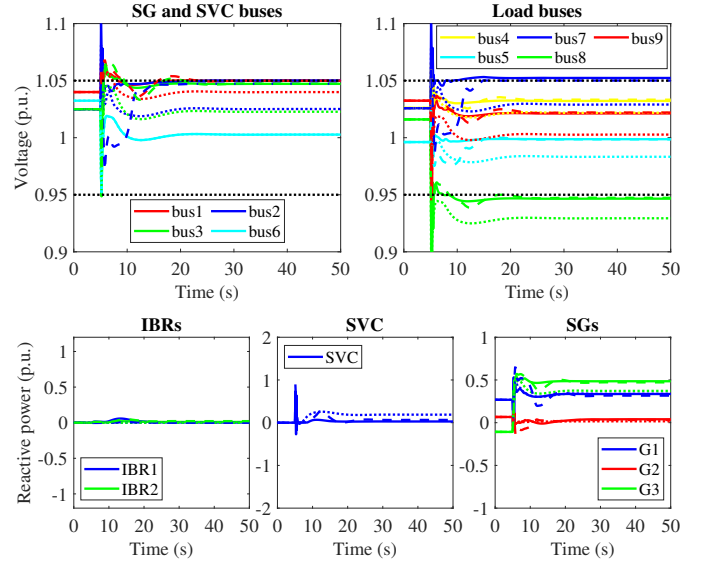


Figure 10: Voltage and reactive power profiles during disturbance in Scenario 7 (dotted: offline (inaccurate), solid: online (inaccurate), dashed: online (accurate))

as in Scenario 1. Here, to enable the proposed controller to tolerate varying large communication delays, we decrease the step size to different values (given in Fig. 11). Fig. 11 shows the voltage and reactive power profiles during disturbance with different communication delays, where the delays from the measurement to the controller and from the controller to the dispatch of set-points are set the same in each case. We observe that the proposed online method can tolerate at least a total of 200 ms communication delays from both the measurements and the dispatch of set-points, with no noticeable performance degradation.

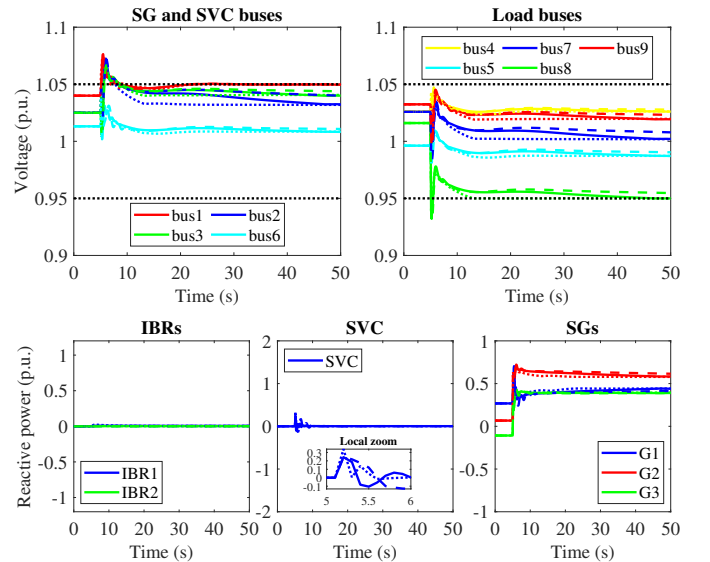


Figure 11: Voltage and reactive power profiles during disturbance in Scenario 8 (dotted: no delay, solid: 50 ms ($\tau = 2 \times 10^{-6}$), dashed: 100 ms ($\tau = 10^{-6}$))

9) *Scenario 9 – Measurement noise test:* To test the impact of measurement noise on the control performance, all measurements are corrupted by white Gaussian noise with varying signal-to-noise ratios (SNR) [32]; the disturbance is the same as in Scenario 1. Fig. 12 shows the voltage and reactive power profiles during disturbance under different SNRs. We observe that the proposed online controller responds effectively and similarly to voltage violations with different measurement noises.

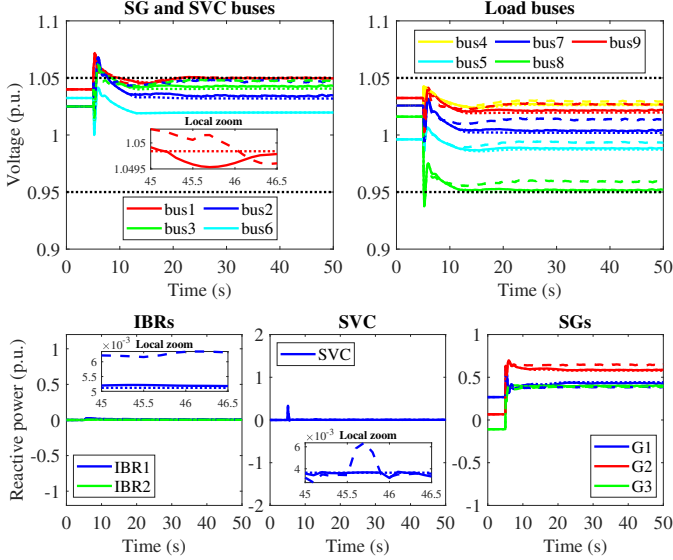


Figure 12: Voltage and reactive power profiles during disturbance in Scenario 9 (dotted: no noise, solid: SNR=60 dB, dashed: SNR=45 dB)

10) *Scenario 10 – Large sampling period test:* We now test the control performance when a larger sampling period is selected (original sampling period is 10 ms); the disturbance is the same as in Scenario 1. Fig. 13 shows the voltage and reactive power profiles during disturbance with sampling periods of 10, 100, and 500 ms. We observe that the proposed controller provides similar performance with large sampling periods.

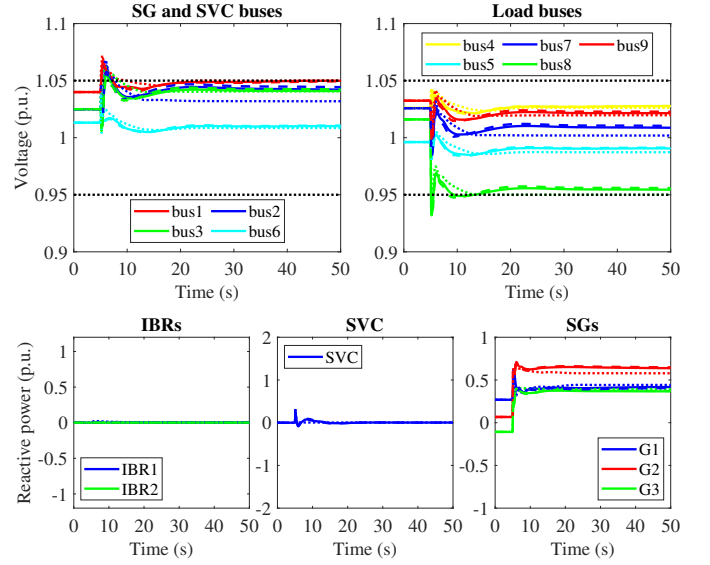


Figure 13: Voltage and reactive power profiles during disturbance in Scenario 10 (dotted: 10 ms, solid: 100 ms, dashed: 500 ms)

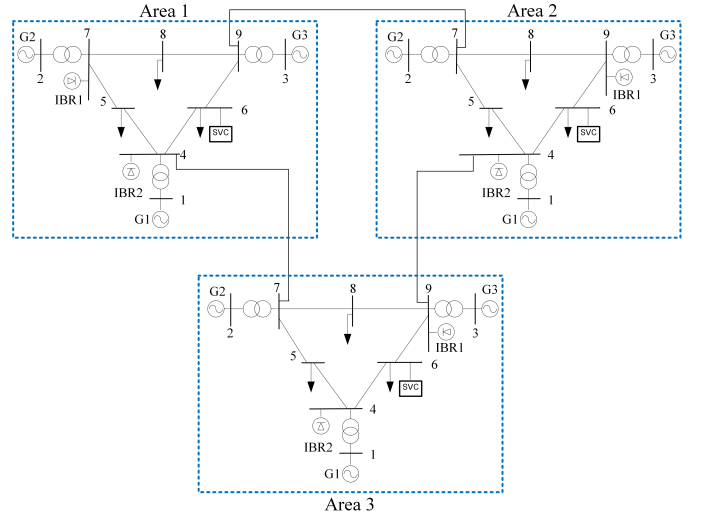


Figure 14: Three-area test system.

B. Three-area System

We now test our controller in a three-area interconnected system shown in Fig. 14, where each area is a copy of the system in Figure 2. The areas are interconnected through identical tie lines, with impedance listed in Table II. The coordinated voltage control scheme is implemented on each area independently; there is no communication of any kind between areas. The control parameters used in each area are the same as the default ones employed in the one-area system, except the weight matrices which are set as $\mathbf{R}_{ibr} = \mathbf{R}_{svc} = \mathbf{R}_{sg} = \mathbf{I}$.

Table II: Tie line parameters.

Resistance (p.u.)	Reactance (p.u.)	Susceptance (p.u.)
0.05	0.20	0.15

1) *Scenario 1 – Basic effectiveness test:* The 120 and 75 MVar reactive power disturbances occur at buses 8 and 7 in Area 1 at $t = 1$ s, respectively, and no disturbance occurs in Area 2 or Area 3. As the control response in Area 3 is similar to that in Area 2, we plot only the results for Areas 1 and 2 in Fig. 15 and Fig. 16, respectively. We observe that the local controllers respond *differently* for the disturbed and non-disturbed areas. In the disturbed area, the local controller eliminates voltage violations by re-dispatching the local resources. In the non-disturbed area, no significant voltage changes occur, and the local controller leaves the device set-points essentially unchanged. We conclude that the proposed approach provides localized control, with no significant inter-area responses; this is desirable, as it is not efficient to transmit reactive power

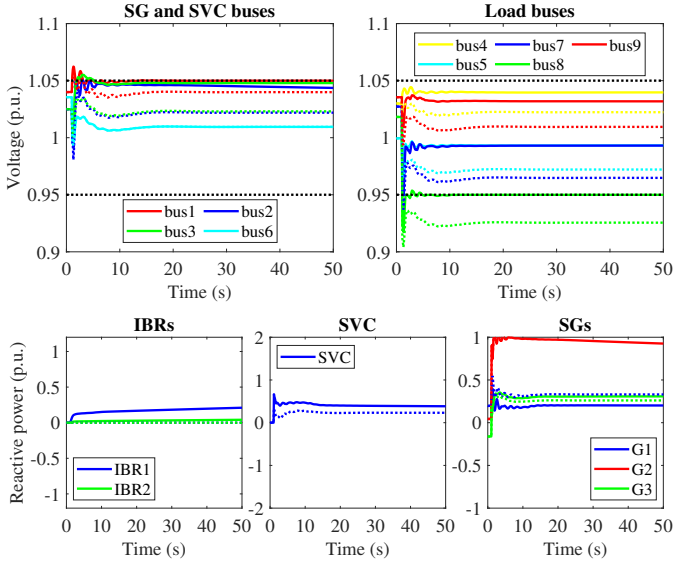


Figure 15: Voltage and reactive power profiles in Area 1 during disturbance (dotted: without control, solid: with control)

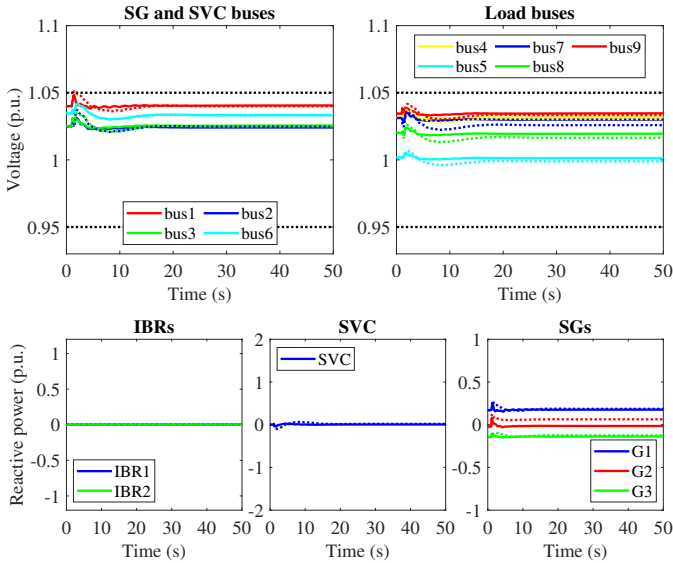


Figure 16: Voltage and reactive power profiles in Area 2 during disturbance (dotted: without control, solid: with control)

over long distances for voltage support.

2) Scenario 2 – Comparison with an offline approach:

We next compare the control performance of the proposed online decentralized approach with that of a global offline approach, as employed in Scenario 6 of Section III-A; the disturbance is the same as in the previous scenario. It should be noted that the offline approach accounts for tie-lines between the areas, while the proposed online approach ignores these connections. Fig. 17, Fig. 18, and Fig. 19 show the voltage and reactive power profiles during disturbance in Area 1, 2, and 3, respectively. The achieved steady-state objective function values of the proposed online approach and offline approach are 1.19 and 1.04, respectively. We observe that the control responses obtained by these two approaches in

Area 1 (disturbed area) are slightly different, due to different sensitivity information employed, but are very similar in Areas 2 and 3 (non-disturbed areas) due to the long tie lines. This echoes the conclusions obtained in the previous scenario and demonstrates the effectiveness of the extension for multi-area systems developed in Section II-G.

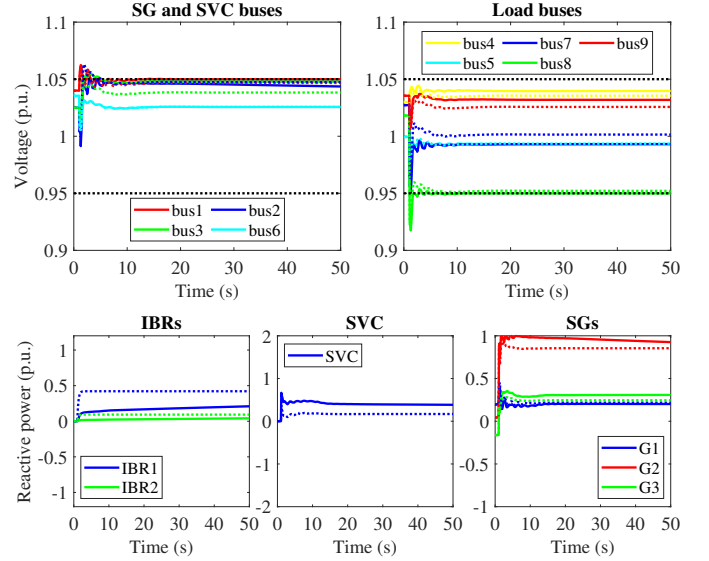


Figure 17: Voltage and reactive power profiles in Area 1 during disturbance (dotted: offline, solid: online)

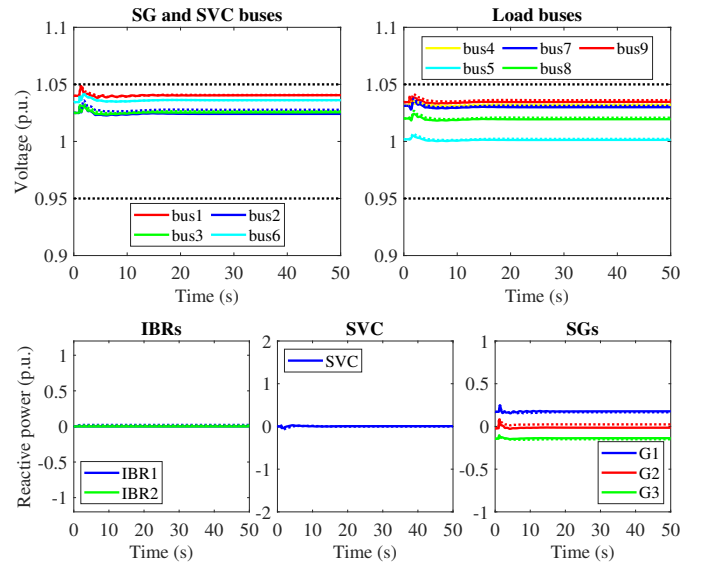


Figure 18: Voltage and reactive power profiles in Area 2 during disturbance (dotted: offline, solid: online)

3) Scenario 3 – Voltage recovery term test: We finally test the effectiveness of the addition of the voltage recovery term described in Section II-F. To this end, we apply a three-phase fault at bus 5 in Area 1 at $t = 5s$ and clear it at $t = 5.2s$. To encourage the reactive outputs of devices come back to their pre-disturbance values quickly, we select large weight matrices $\mathbf{R}_{ibr} = \mathbf{R}_{svc} = 100\mathbf{I}$, $\mathbf{R}_{sg} = 10\mathbf{I}$. The weight matrix \mathbf{R}_v in

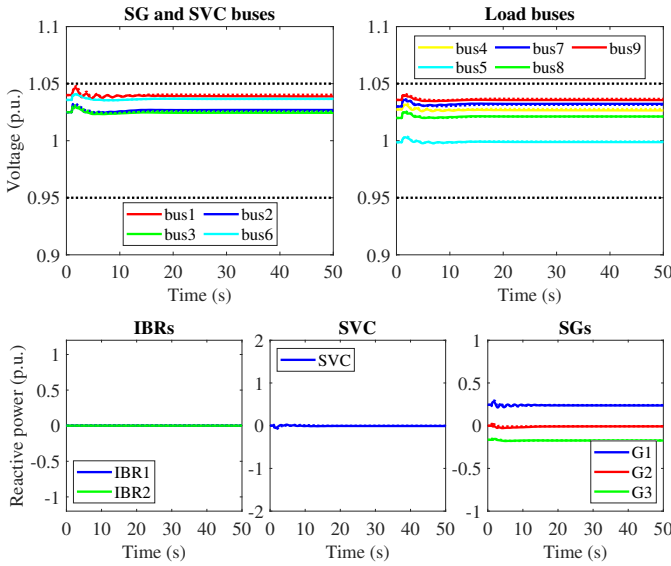


Figure 19: Voltage and reactive power profiles in Area 3 during disturbance (dotted: offline, solid: online)

(12) is set as $100I$. Fig. 20 shows the voltage and reactive power profiles during disturbance in Area 1 without and with the additional voltage recovery term. From Fig. 20, we see that both the voltages and reactive power outputs of all control devices come back to their pre-disturbance points with the additional voltage deviation penalty term.

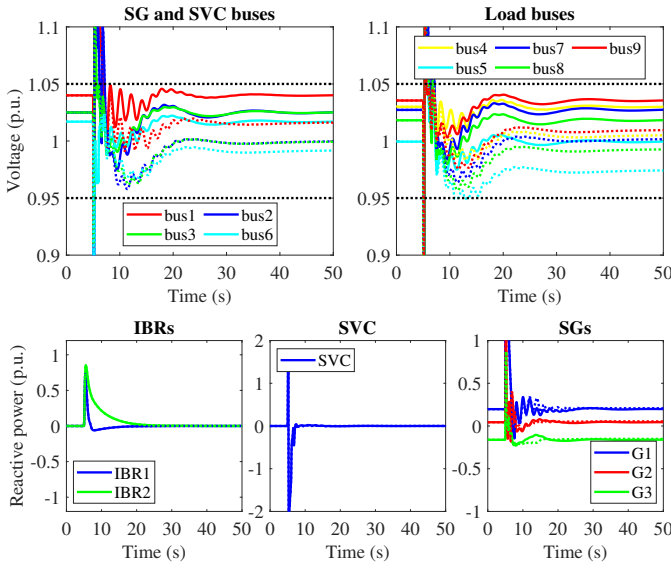


Figure 20: Voltage and reactive power profiles in Area 1 during disturbance (dotted: without, solid: with)

IV. CONCLUSIONS

We have proposed a real-time measurement-based coordinated voltage control strategy for transmission systems. The proposed algorithm coordinates IBRs with conventional devices SGs and SVCs to regulate voltages within operational bounds while respecting device limits and optimizing the

usage of reactive power. The controller is simple to implement and tune, requires only minimal grid model information, and leverages real-time feedback to provide robustness against model uncertainty and unmeasured disturbances. Extensive simulations have been presented validating the method. Finally, while the algorithm is primarily designed for grid support during normal operating conditions, simulation results indicate that it can also improve system performance during more severe events such as FIDVR.

REFERENCES

- [1] H. Sun, Q. Guo, J. Qi, V. Ajarapu, R. Bravo, J. Chow, Z. Li, R. Moghe, E. Nasr-Azadani, U. Tamrakar, *et al.*, “Review of challenges and research opportunities for voltage control in smart grids,” *IEEE Transactions on Power Systems*, vol. 34, no. 4, pp. 2790–2801, 2019.
- [2] Q. Guo, H. Sun, B. Wang, B. Zhang, W. Wu, and L. Tang, “Hierarchical automatic voltage control for integration of large-scale wind power: Design and implementation,” *Electric Power Systems Research*, vol. 120, pp. 234–241, 2015.
- [3] Y. Zhang, Y. Xu, Z. Y. Dong, and P. Zhang, “Real-time assessment of fault-induced delayed voltage recovery: A probabilistic self-adaptive data-driven method,” *IEEE Transactions on Smart Grid*, vol. 10, no. 3, pp. 2485–2494, 2018.
- [4] H. Zhao, Q. Wu, Q. Guo, H. Sun, S. Huang, and Y. Xue, “Coordinated voltage control of a wind farm based on model predictive control,” *IEEE Transactions on Sustainable Energy*, vol. 7, no. 4, pp. 1440–1451, 2016.
- [5] S. Bolognani, R. Carli, G. Cavraro, and S. Zampieri, “Distributed reactive power feedback control for voltage regulation and loss minimization,” *IEEE Transactions on Automatic Control*, vol. 60, no. 4, pp. 966–981, 2014.
- [6] S. Corsi, M. Pozzi, C. Sabelli, and A. Serrani, “The coordinated automatic voltage control of the italian transmission grid-part i: Reasons of the choice and overview of the consolidated hierarchical system,” *IEEE Transactions on Power Systems*, vol. 19, no. 4, pp. 1723–1732, 2004.
- [7] H. Sun, Q. Guo, B. Zhang, W. Wu, and B. Wang, “An adaptive zone-division-based automatic voltage control system with applications in china,” *IEEE Transactions on Power Systems*, vol. 28, no. 2, pp. 1816–1828, 2012.
- [8] B. Zhao, C. Guo, and Y. Cao, “A multiagent-based particle swarm optimization approach for optimal reactive power dispatch,” *IEEE Transactions on Power Systems*, vol. 20, no. 2, pp. 1070–1078, 2005.
- [9] S. H. Low, “Convex relaxation of optimal power flow—part i: Formulations and equivalence,” *IEEE Transactions on Control of Network Systems*, vol. 1, no. 1, pp. 15–27, 2014.
- [10] M. Colombino, J. W. Simpson-Porco, and A. Bernstein, “Towards robustness guarantees for feedback-based optimization,” in *IEEE Conf. on Decision and Control*, (Nice, France), pp. 6207–6214, Dec. 2019.
- [11] N.-c. CHANG, Z. Lan, D.-q. GAN, and Y.-x. NI, “A survey on applications of wide-area measurement system in power system analysis and control [j],” *Power System Technology*, vol. 10, pp. 47–50, 2005.
- [12] H. Chen, T. Jiang, H. Yuan, H. Jia, L. Bai, and F. Li, “Wide-area measurement-based voltage stability sensitivity and its application in voltage control,” *International Journal of Electrical Power & Energy Systems*, vol. 88, pp. 87–98, 2017.
- [13] M. Glavic and T. Van Cutsem, “A short survey of methods for voltage instability detection,” in *2011 IEEE Power and Energy Society General Meeting*, pp. 1–8, IEEE, 2011.
- [14] H.-Y. Su, F.-M. Kang, and C.-W. Liu, “Transmission grid secondary voltage control method using pmu data,” *IEEE Transactions on Smart Grid*, vol. 9, no. 4, pp. 2908–2917, 2016.
- [15] H.-Y. Su and C.-W. Liu, “An adaptive pmu-based secondary voltage control scheme,” *IEEE Transactions on Smart Grid*, vol. 4, no. 3, pp. 1514–1522, 2013.
- [16] A. Morattab, O. Akhrif, and M. Saad, “Decentralised coordinated secondary voltage control of multi-area power grids using model predictive control,” *IET Generation, Transmission & Distribution*, vol. 11, no. 18, pp. 4546–4555, 2017.
- [17] H. Xu, A. D. Domínguez-García, V. V. Veeravalli, and P. W. Sauer, “Data-driven voltage regulation in radial power distribution systems,” *IEEE Transactions on Power Systems*, vol. 35, no. 3, pp. 2133–2143, 2019.

- [18] H. Su, P. Li, X. Fu, L. Yu, and C. Wang, "Augmented sensitivity estimation based voltage control strategy of active distribution networks with pmu measurement," *IEEE Access*, vol. 7, pp. 44987–44997, 2019.
- [19] H. Xu, A. D. Domínguez-García, and P. W. Sauer, "Data-driven coordination of distributed energy resources for active power provision," *IEEE Transactions on Power Systems*, vol. 34, no. 4, pp. 3047–3058, 2019.
- [20] S. Nowak, C. Chen, and L. Wang, "Measurement-based optimal der dispatch with a recursively estimated sensitivity model," *IEEE Transactions on Power Systems*, 2020.
- [21] L. Ortmann, A. Hauswirth, I. Caduff, F. Dörfler, and S. Bolognani, "Experimental validation of feedback optimization in power distribution grids," *Electric Power Systems Research*, vol. 189, p. 106782, 2020.
- [22] G. Qu and N. Li, "Optimal distributed feedback voltage control under limited reactive power," *IEEE Transactions on Power Systems*, vol. 35, no. 1, pp. 315–331, 2019.
- [23] C.-Y. Chang, M. Colombino, J. Corté, and E. Dall'Anese, "Saddle-flow dynamics for distributed feedback-based optimization," *IEEE Control Systems Letters*, vol. 3, no. 4, pp. 948–953, 2019.
- [24] E. Dall'Anese and A. Simonetto, "Optimal power flow pursuit," *IEEE Transactions on Smart Grid*, vol. 9, no. 2, pp. 942–952, 2016.
- [25] A. Bernstein and E. Dall'Anese, "Real-time feedback-based optimization of distribution grids: A unified approach," *IEEE Transactions on Control of Network Systems*, vol. 6, no. 3, pp. 1197–1209, 2019.
- [26] T. Boehme, A. R. Wallace, and G. P. Harrison, "Applying time series to power flow analysis in networks with high wind penetration," *IEEE transactions on power systems*, vol. 22, no. 3, pp. 951–957, 2007.
- [27] L. Lessard, B. Recht, and A. Packard, "Analysis and design of optimization algorithms via integral quadratic constraints," *SIAM Journal on Optimization*, vol. 26, no. 1, pp. 57–95, 2016.
- [28] E. J. Davison, "Multivariable tuning regulators: The feedforward and robust control of a general servomechanism problem," *IEEE Transactions on Automatic Control*, vol. 21, no. 1, pp. 35–47, 1976.
- [29] A. Delavari, I. Kamwa, and P. Brunelle, "Simscape power systems benchmarks for education and research in power grid dynamics and control," in *2018 IEEE Canadian Conference on Electrical & Computer Engineering (CCECE)*, pp. 1–5, IEEE, 2018.
- [30] P. M. Anderson and A. A. Fouad, *Power system control and stability*. John Wiley & Sons, 2008.
- [31] H. Bai and V. Ajjarapu, "A novel online load shedding strategy for mitigating fault-induced delayed voltage recovery," *IEEE Transactions on Power Systems*, vol. 26, no. 1, pp. 294–304, 2010.
- [32] S. Nowak, C. Chen, and L. Wang, "Measurement-based optimal der dispatch with a recursively estimated sensitivity model," *IEEE Transactions on Power Systems*, 2020.
- [33] J. W. Simpson-Porco and F. Bullo, "Distributed monitoring of voltage collapse sensitivity indices," *IEEE Transactions on Smart Grid*, vol. 7, no. 4, pp. 1979–1988, 2016.
- [34] H. H. Bauschke and P. L. Combettes, *Convex Analysis and Monotone Operator Theory in Hilbert Spaces*. Springer, 1 ed., 2011.
- [35] N. Bof, R. Carli, and L. Schnato, "Lyapunov theory for discrete time systems." <https://arxiv.org/abs/1809.05289>.

APPENDIX A COMPUTATION OF SENSITIVITY MATRICES

Given the nonlinear power flow equations, around an operating point, the incremental changes in phase angle at all buses $\Delta\theta$, load bus voltages Δv_l , and voltage-regulated bus voltages Δv_t are related to incremental changes in active power injections at all buses Δp , reactive power injections at load buses Δq_l , and reactive power injections at voltage-regulated buses Δq_t by

$$\begin{bmatrix} \Delta p \\ \Delta q_l \\ \Delta q_t \end{bmatrix} = \begin{bmatrix} J_{p\theta} & J_{pv_l} & J_{pv_t} \\ J_{q_l\theta} & J_{q_lv_l} & J_{q_lv_t} \\ J_{q_t\theta} & J_{q_tv_l} & J_{q_tv_t} \end{bmatrix} \begin{bmatrix} \Delta\theta \\ \Delta v_l \\ \Delta v_t \end{bmatrix} \quad (13)$$

where, for example, $J_{p\theta}$ denotes the partial derivative of p with respect to θ , and all partial derivatives are evaluated at the operating point. If variations in Δp and Δv_t are held at

zero, the first two block rows in (13) can be solved to yield [33]:

$$\frac{\Delta q_l}{\Delta v_l} = J_{q_lv_l} - J_{q_l\theta} J_{p\theta}^\dagger J_{pv_l} \quad (14)$$

where \dagger denotes the pseudoinverse. It follows that

$$\frac{\Delta v_l}{\Delta q_l} = \left(\frac{\Delta q_l}{\Delta v_l} \right)^{-1} = (J_{q_lv_l} - J_{q_l\theta} J_{p\theta}^\dagger J_{pv_l})^{-1}. \quad (15)$$

Setting $\Delta p = \mathbf{0}$ and $\Delta q_l = \mathbf{0}$ in (13) and eliminating $\Delta\theta$ in first two block rows of (13), we obtain

$$\mathbf{0} = \frac{\Delta q_l}{\Delta v_l} \Delta v_l + \frac{\Delta q_t}{\Delta v_t} \Delta v_t \quad (16)$$

where

$$\frac{\Delta q_t}{\Delta v_t} = J_{q_tv_t} - J_{q_t\theta} J_{p\theta}^\dagger J_{pv_t}. \quad (17)$$

From (16), we obtain

$$\frac{\Delta v_l}{\Delta v_t} = -\frac{\Delta v_l}{\Delta q_l} \cdot \frac{\Delta q_l}{\Delta v_t}. \quad (18)$$

Similarly, setting $\Delta p = \mathbf{0}$ and $\Delta v_t = \mathbf{0}$ in (13) and eliminating $\Delta\theta$ in last two block rows of (13) obtains [33]

$$\Delta q_l = \frac{\Delta q_l}{\Delta v_l} \Delta v_l, \quad \Delta q_t = \frac{\Delta q_t}{\Delta v_l} \Delta v_l \quad (19)$$

where $\frac{\Delta q_t}{\Delta v_l}$ is defined as

$$\frac{\Delta q_t}{\Delta v_l} = J_{q_tv_l} - J_{q_t\theta} J_{p\theta}^\dagger J_{pv_l}. \quad (20)$$

Eliminating Δv_l from this pair in (19) gives

$$\frac{\Delta q_t}{\Delta q_l} = \frac{\Delta q_t}{\Delta v_l} \left(\frac{\Delta q_l}{\Delta v_l} \right)^{-1}. \quad (21)$$

Again, setting $\Delta p = \mathbf{0}$ and $\Delta q_t = \mathbf{0}$ in (13) and eliminating $\Delta\theta$ in the first and last block rows of (13) to obtain

$$\mathbf{0} = \frac{\Delta q_t}{\Delta v_l} \Delta v_l + \frac{\Delta q_t}{\Delta v_t} \Delta v_t \quad (22)$$

where $\frac{\Delta q_t}{\Delta v_t}$ is defined as

$$\frac{\Delta q_t}{\Delta v_t} = J_{q_tv_t} - J_{q_t\theta} J_{p\theta}^\dagger J_{pv_t}. \quad (23)$$

The sensitivity matrices $\mathbf{\Pi}$ in (8) can now be constructed based on the above. To construct $\mathbf{\Pi}_1$, the component $\frac{\partial q_{ibr}}{\partial q_{ibr}} = \mathbf{I}$ and the component $\frac{\partial q_{ibr}}{\partial v_t} = [\frac{\partial q_{ibr}}{\partial v_{sg}}, \frac{\partial q_{ibr}}{\partial v_{svc}}] = [\mathbf{0}, \mathbf{0}]$. This is because the reactive power outputs of IBRs are only affected by their reactive power set-points. The component $\frac{\partial q_t}{\partial q_{ibr}}$ can be obtained from $\frac{\Delta q_t}{\Delta q_l}$ in (21) by selecting the corresponding columns with respect to buses attached to IBRs. And the component $\frac{\partial q_t}{\partial v_t}$ can be obtained from $\frac{\Delta q_t}{\Delta v_t}$ in (23), that is $\frac{\partial q_t}{\partial v_t} = \frac{\Delta q_t}{\Delta v_t}$. To construct $\mathbf{\Pi}_2$, the component $\frac{\partial v_l}{\partial q_{ibr}}$ can be obtained from $\frac{\Delta v_l}{\Delta q_l}$ in (15) by selecting the corresponding columns with respect to buses attached to IBRs, whereas the component $\frac{\partial v_l}{\partial v_t}$ can be obtained from $\frac{\Delta v_l}{\Delta v_t}$ in (18), that is $\frac{\partial v_l}{\partial v_t} = \frac{\Delta v_l}{\Delta v_t}$. The components of matrix $\mathbf{\Pi}_3$ have already been obtained as sub-components of $\mathbf{\Pi}_1$.

APPENDIX B
PROOF OF THEOREM II.2

The proof is based on a composite Lyapunov construction, and is divided into several steps.

Step #1 — Equilibrium and Error Equations: Let $\mathbf{w} \in \mathcal{W}$. Closed-loop equilibria $(\bar{\mathbf{x}}, \bar{\mathbf{u}})$ are characterized by

$$\begin{aligned}\bar{\mathbf{x}} &= \mathbf{f}(\bar{\mathbf{x}}, \bar{\mathbf{u}}, \mathbf{w}) \\ \bar{\mathbf{y}} &\triangleq (\bar{\mathbf{q}}, \bar{\mathbf{v}}_1) = \mathbf{h}(\bar{\mathbf{x}}, \bar{\mathbf{u}}, \mathbf{w}) \\ \mathbf{0} &= \mathbf{F}(\bar{\mathbf{y}}).\end{aligned}\quad (24)$$

Given any $\bar{\mathbf{u}} \in \mathcal{V}$, it follows from (A2) that the first equation in (24) can be solved for $\bar{\mathbf{x}} = \pi_x(\bar{\mathbf{u}}, \mathbf{w})$, which by local exponential stability (A3) must be an isolated equilibrium. Eliminating $\bar{\mathbf{x}}$ and $\bar{\mathbf{y}}$ and recalling that $\pi_{\text{ps}}(\mathbf{u}, \mathbf{w}) = \mathbf{h}(\pi_x(\mathbf{u}, \mathbf{w}), \mathbf{u}, \mathbf{w})$, we obtain the reduced equilibrium equation

$$\mathbf{0} = \mathbf{F}(\pi_{\text{ps}}(\bar{\mathbf{u}}, \mathbf{w})). \quad (25)$$

Since both \mathbf{F} and π_{ps} are continuous, it follows from (A4) that there exists a unique $\bar{\mathbf{u}} \in \mathcal{V}$ satisfying (25) [34, Example 22.9]. We conclude that the closed-loop system possess a unique equilibrium point $(\bar{\mathbf{x}}, \bar{\mathbf{u}}) \in \mathcal{X} \times \mathcal{V}$ with associated measurements $\bar{\mathbf{y}} = \mathbf{h}(\bar{\mathbf{x}}, \bar{\mathbf{u}}, \mathbf{w})$. Consider now the change of state variable

$$\boldsymbol{\xi}^k \triangleq \mathbf{x}^k - \pi_x(\mathbf{u}^k, \mathbf{w}).$$

In these error coordinates, the dynamics (9),(6),(7) become

$$\begin{aligned}\boldsymbol{\xi}^{k+1} &= \mathbf{f}(\boldsymbol{\xi}^k + \pi_x(\mathbf{u}^k, \mathbf{w}), \mathbf{u}^k, \mathbf{w}) - \pi_x(\mathbf{u}^{k+1}, \mathbf{w}) \\ \mathbf{y}^k &= \mathbf{h}(\boldsymbol{\xi}^k + \pi_x(\mathbf{u}^k, \mathbf{w}), \mathbf{u}^k, \mathbf{w}) \\ \mathbf{u}^{k+1} &= \mathbf{u}^k - \tau \mathbf{F}(\mathbf{y}^k),\end{aligned}\quad (26)$$

and the equilibrium point of interest is $(\boldsymbol{\xi}, \mathbf{u}) = (0, \bar{\mathbf{u}})$.

Step #2 — Analyzing the Slow Dynamics: With $V_s(\mathbf{u}) = \|\mathbf{u} - \bar{\mathbf{u}}\|_2^2$ we compute that

$$\begin{aligned}V_s(\mathbf{u}^{k+1}) &= \|\mathbf{u}^k - \bar{\mathbf{u}} - \tau \mathbf{F}(\mathbf{y}^k)\|_2^2 \\ &= \|\mathbf{u}^k - \bar{\mathbf{u}} - \tau \mathbf{F}(\pi_{\text{ps}}(\mathbf{u}^k, \mathbf{w})) \\ &\quad - \tau [\mathbf{F}(\mathbf{y}^k) - \mathbf{F}(\pi_{\text{ps}}(\mathbf{u}^k, \mathbf{w}))]\|_2^2\end{aligned}$$

where we added and subtracted $\tau \mathbf{F}(\pi_{\text{ps}}(\mathbf{u}^k, \mathbf{w}))$ inside the norm. Expanding and bounding, we find that

$$V_s(\mathbf{u}^{k+1}) \leq \delta_1^2 + 2\tau\delta_1\delta_2 + \tau^2\delta_2^2$$

where

$$\begin{aligned}\delta_1 &= \|\mathbf{u}^k - \bar{\mathbf{u}} - \tau \mathbf{F}(\pi_{\text{ps}}(\mathbf{u}^k, \mathbf{w}))\|_2 \\ \delta_2 &= \|\mathbf{F}(\mathbf{y}^k) - \mathbf{F}(\pi_{\text{ps}}(\mathbf{u}^k, \mathbf{w}))\|_2.\end{aligned}$$

By (A4) there exists $\mu > 0$ such that $[\mathbf{F}(\pi_{\text{ps}}(\mathbf{u}_1, \mathbf{w})) - \mathbf{F}(\pi_{\text{ps}}(\mathbf{u}_2, \mathbf{w}))]^\top(\mathbf{u}_1 - \mathbf{u}_2) \geq \mu\|\mathbf{u}_1 - \mathbf{u}_2\|_2^2$ for all $\mathbf{u}_1, \mathbf{u}_2 \in \mathcal{V}$ and all $\mathbf{w} \in \mathcal{W}$. Let L_F and L_π denote the respective Lipschitz continuity parameters of \mathbf{F} and π_{ps} . Then

$$\begin{aligned}\delta_1^2 &= \|\mathbf{u}^k - \bar{\mathbf{u}}\|_2^2 + \tau^2\|\mathbf{F}(\pi_{\text{ps}}(\mathbf{u}^k, \mathbf{w}))\|_2^2 \\ &\quad - 2\tau(\mathbf{u}^k - \bar{\mathbf{u}})^\top \mathbf{F}(\pi_{\text{ps}}(\mathbf{u}^k, \mathbf{w})) \\ &= \|\mathbf{u}^k - \bar{\mathbf{u}}\|_2^2 + \tau^2\|\mathbf{F}(\pi_{\text{ps}}(\mathbf{u}^k, \mathbf{w})) - \mathbf{F}(\pi_{\text{ps}}(\bar{\mathbf{u}}, \mathbf{w}))\|_2^2 \\ &\quad - 2\tau(\mathbf{u}^k - \bar{\mathbf{u}})^\top (\mathbf{F}(\pi_{\text{ps}}(\mathbf{u}^k, \mathbf{w})) - \mathbf{F}(\pi_{\text{ps}}(\bar{\mathbf{u}}, \mathbf{w}))) \\ &\leq \underbrace{(1 - 2\tau\mu + \tau^2 L_F^2 L_\pi^2)}_{\triangleq c^2} \|\mathbf{u}^k - \bar{\mathbf{u}}\|_2^2\end{aligned}$$

where we used that $\mathbf{0} = \mathbf{F}(\pi_{\text{ps}}(\bar{\mathbf{u}}, \mathbf{w}))$. Note that if $\tau \in (0, 2\mu/(L_F L_\pi)^2)$, then $c \in (0, 1)$. We next bound δ_2 as

$$\begin{aligned}\delta_2 &\leq L_F \|\mathbf{y}^k - \pi_{\text{ps}}(\mathbf{u}^k, \mathbf{w})\|_2 \\ &= L_F \|\mathbf{h}(\boldsymbol{\xi}^k + \pi_x(\mathbf{u}^k, \mathbf{w}), \mathbf{u}^k, \mathbf{w}) - \mathbf{h}(\pi_x(\mathbf{u}^k, \mathbf{w}), \mathbf{u}^k, \mathbf{w})\|_2 \\ &\leq L_F L_h \|\boldsymbol{\xi}^k\|_2\end{aligned}$$

where L_h is the Lipschitz constant of \mathbf{h} . Combining these inequalities, we find that

$$V_s(\mathbf{u}^{k+1}) - V_s(\mathbf{u}^k) \leq (\boldsymbol{\zeta}^k)^\top Q_s \boldsymbol{\zeta}^k$$

where $\boldsymbol{\zeta}^k = (\|\boldsymbol{\xi}^k\|_2, \|\mathbf{u}^k - \bar{\mathbf{u}}\|_2)$ and

$$Q_s = \begin{bmatrix} q_1 \tau^2 & \tau c q_2 \\ \tau c q_2 & -(1 - c^2) \end{bmatrix}.$$

where $q_1, q_2 > 0$ are constants which can be determined from the above and are independent of τ .

Step #3 — Analyzing the Fast Dynamics: Define the deviation vector field $\mathbf{g} : \mathbb{R}^n \times \mathcal{V} \times \mathcal{W} \rightarrow \mathbb{R}^n$ by

$$\begin{aligned}\mathbf{g}(\boldsymbol{\xi}, \mathbf{u}, \mathbf{w}) &= \mathbf{f}(\boldsymbol{\xi} + \pi_x(\mathbf{u}, \mathbf{w}), \mathbf{u}, \mathbf{w}) - \mathbf{f}(\pi_x(\mathbf{u}, \mathbf{w}), \mathbf{u}, \mathbf{w}) \\ &= \mathbf{f}(\boldsymbol{\xi} + \pi_x(\mathbf{u}, \mathbf{w}), \mathbf{u}, \mathbf{w}) - \pi_x(\mathbf{u}, \mathbf{w}).\end{aligned}$$

Assumptions (A1)–(A3) are sufficient to invoke the discrete converse Lyapunov theorem for uniform exponential stability (e.g., [35, Sec. 6]), which states that there exists a set \mathcal{Z} containing the origin in its interior, positive constants $c_1, c_2, c_3, c_4 > 0$, $\rho_f \in [0, 1)$, and a continuous function

$$V_f : \mathcal{Z} \times \mathcal{V} \times \mathcal{W} \rightarrow \mathbb{R}_{\geq 0}, \quad (\boldsymbol{\xi}, \mathbf{u}, \mathbf{w}) \mapsto V_f(\boldsymbol{\xi}, \mathbf{u}, \mathbf{w})$$

satisfying the conditions

$$c_1 \|\boldsymbol{\xi}\|_2^2 \leq V_f(\boldsymbol{\xi}, \mathbf{u}, \mathbf{w}) \leq c_2 \|\boldsymbol{\xi}\|_2^2 \quad (27a)$$

$$V_f(\mathbf{g}(\boldsymbol{\xi}, \mathbf{u}, \mathbf{w}), \mathbf{u}, \mathbf{w}) - V_f(\boldsymbol{\xi}, \mathbf{u}, \mathbf{w}) \leq -\rho_f \|\boldsymbol{\xi}\|_2^2 \quad (27b)$$

$$|V_f(\boldsymbol{\xi}, \mathbf{u}, \mathbf{w}) - V_f(\boldsymbol{\xi}', \mathbf{u}, \mathbf{w})| \leq c_3 (\|\boldsymbol{\xi}\|_2 + \|\boldsymbol{\xi}'\|_2) \|\boldsymbol{\xi} - \boldsymbol{\xi}'\|_2 \quad (27c)$$

$$|V_f(\boldsymbol{\xi}, \mathbf{u}, \mathbf{w}) - V_f(\boldsymbol{\xi}, \mathbf{u}', \mathbf{w})| \leq c_4 \|\boldsymbol{\xi}\|_2^2 \|\mathbf{u} - \mathbf{u}'\|_2 \quad (27d)$$

for all $\boldsymbol{\xi}, \boldsymbol{\xi}' \in \mathcal{Z}$, all $\mathbf{u}, \mathbf{u}' \in \mathcal{V}$, and all $\mathbf{w} \in \mathcal{W}$. Let

$$\Delta V_f = V_f(\boldsymbol{\xi}^{k+1}, \mathbf{u}^{k+1}, \mathbf{w}) - V_f(\boldsymbol{\xi}^k, \mathbf{u}^k, \mathbf{w})$$

denote the incremental change in V_f along trajectories of (26). Substituting in the dynamics (26) and adding and subtracting terms, we can express the overall change as

$$\Delta V_f = \Delta V_f^1 + \Delta V_f^2 + \Delta V_f^3, \quad (28)$$

where the individual summands are defined in (29).

We now bound each term in (28) individually. Applying (27c) to $|\Delta V_f^1|$ we obtain

$$\begin{aligned}|\Delta V_f^1| &\leq c_3 \|\pi_x(\mathbf{u}^{k+1}, \mathbf{w}) - \pi_x(\mathbf{u}^k, \mathbf{w})\|_2 \\ &\quad \cdot \left(\|\mathbf{f}(\boldsymbol{\xi}^k + \pi_x(\mathbf{u}^k, \mathbf{w}), \mathbf{u}^k, \mathbf{w}) - \pi_x(\mathbf{u}^{k+1}, \mathbf{w})\|_2 \right. \\ &\quad \left. + \|\mathbf{f}(\boldsymbol{\xi}^k + \pi_x(\mathbf{u}^k, \mathbf{w}), \mathbf{u}^k, \mathbf{w}) - \pi_x(\mathbf{u}^k, \mathbf{w})\|_2 \right)\end{aligned}\quad (30)$$

Since π_x is Lipschitz continuous we have

$$\|\pi_x(\mathbf{u}^{k+1}, \mathbf{w}) - \pi_x(\mathbf{u}^k, \mathbf{w})\|_2 \leq L_{\pi_x} \|\mathbf{u}^{k+1} - \mathbf{u}^k\|_2. \quad (31)$$

$$\begin{aligned}
\Delta V_f^1 &\triangleq V_f(\mathbf{f}(\boldsymbol{\xi}^k + \boldsymbol{\pi}_x(\mathbf{u}^k, \mathbf{w}), \mathbf{u}^k, \mathbf{w}) - \boldsymbol{\pi}_x(\mathbf{u}^{k+1}, \mathbf{w}), \mathbf{u}^{k+1}, \mathbf{w}) \\
&\quad - V_f(\mathbf{f}(\boldsymbol{\xi}^k + \boldsymbol{\pi}_x(\mathbf{u}^k, \mathbf{w}), \mathbf{u}^k, \mathbf{w}) - \boldsymbol{\pi}_x(\mathbf{u}^k, \mathbf{w}), \mathbf{u}^{k+1}, \mathbf{w}) \\
\Delta V_f^2 &\triangleq V_f(\mathbf{f}(\boldsymbol{\xi}^k + \boldsymbol{\pi}_x(\mathbf{u}^k, \mathbf{w}), \mathbf{u}^k, \mathbf{w}) - \boldsymbol{\pi}_x(\mathbf{u}^k, \mathbf{w}), \mathbf{u}^{k+1}, \mathbf{w}) \\
&\quad - V_f(\mathbf{f}(\boldsymbol{\xi}^k + \boldsymbol{\pi}_x(\mathbf{u}^k, \mathbf{w}), \mathbf{u}^k, \mathbf{w}) - \boldsymbol{\pi}_x(\mathbf{u}^k, \mathbf{w}), \mathbf{u}^k, \mathbf{w}) \\
\Delta V_f^3 &\triangleq V_f(\mathbf{f}(\boldsymbol{\xi}^k + \boldsymbol{\pi}_x(\mathbf{u}^k, \mathbf{w}), \mathbf{u}^k, \mathbf{w}) - \boldsymbol{\pi}_x(\mathbf{u}^k, \mathbf{w}), \mathbf{u}^k, \mathbf{w}) - V_f(\boldsymbol{\xi}^k, \mathbf{u}^k, \mathbf{w}).
\end{aligned} \tag{29}$$

Since $\boldsymbol{\pi}_x(\mathbf{u}, \mathbf{w}) = \mathbf{f}(\boldsymbol{\pi}_x(\mathbf{u}, \mathbf{w}), \mathbf{u}, \mathbf{w})$ and \mathbf{f} is Lipschitz continuous in its first argument uniformly in (\mathbf{u}, \mathbf{w}) , we have

$$\begin{aligned}
&\|\mathbf{f}(\boldsymbol{\xi}^k + \boldsymbol{\pi}_x(\mathbf{u}^k, \mathbf{w}), \mathbf{u}^k, \mathbf{w}) - \boldsymbol{\pi}_x(\mathbf{u}^{k+1}, \mathbf{w})\|_2 \\
&= \|\mathbf{f}(\boldsymbol{\xi}^k + \boldsymbol{\pi}_x(\mathbf{u}^k, \mathbf{w}), \mathbf{u}^k, \mathbf{w}) - \mathbf{f}(\boldsymbol{\pi}_x(\mathbf{u}^{k+1}, \mathbf{w}), \mathbf{u}^{k+1}, \mathbf{w})\|_2 \\
&\leq L_f \sqrt{\|\boldsymbol{\xi}^k + \boldsymbol{\pi}_x(\mathbf{u}^k, \mathbf{w}) - \boldsymbol{\pi}_x(\mathbf{u}^{k+1}, \mathbf{w})\|_2^2 + \|\mathbf{u}^{k+1} - \mathbf{u}^k\|_2^2} \\
&\leq L_f \|\boldsymbol{\xi}^k\|_2 + L_f(1 + L_{\boldsymbol{\pi}_x}) \|\mathbf{u}^{k+1} - \mathbf{u}^k\|_2
\end{aligned} \tag{32}$$

and that

$$\|\mathbf{f}(\boldsymbol{\xi}^k + \boldsymbol{\pi}_x(\mathbf{u}^k, \mathbf{w}), \mathbf{u}^k, \mathbf{w}) - \boldsymbol{\pi}_x(\mathbf{u}^k, \mathbf{w})\|_2 \leq L_f \|\boldsymbol{\xi}^k\|_2. \tag{33}$$

Substituting (31)–(33) back into (30), we obtain

$$\begin{aligned}
|\Delta V_f^1| &\leq c_3 L_f L_{\boldsymbol{\pi}_x} (1 + L_{\boldsymbol{\pi}_x}) \|\mathbf{u}^{k+1} - \mathbf{u}^k\|_2^2 \\
&\quad + 2c_3 L_{\boldsymbol{\pi}_x} L_f \|\boldsymbol{\xi}^k\|_2 \|\mathbf{u}^{k+1} - \mathbf{u}^k\|_2.
\end{aligned} \tag{34}$$

Using (26) and (24) we can obtain the bound

$$\begin{aligned}
\|\mathbf{u}^{k+1} - \mathbf{u}^k\|_2 &= \tau \|\mathbf{F}(\mathbf{y}^k)\|_2 \\
&= \tau \|\mathbf{F}(\mathbf{y}^k) - \mathbf{F}(\bar{\mathbf{y}})\|_2 \\
&\leq \tau L_F \|\mathbf{y}^k - \bar{\mathbf{y}}\|_2 \\
&\leq \tau L_F \|\mathbf{h}(\boldsymbol{\xi}^k + \boldsymbol{\pi}_x(\mathbf{u}^k, \mathbf{w}), \mathbf{u}^k, \mathbf{w}) \\
&\quad - \mathbf{h}(\boldsymbol{\pi}_x(\bar{\mathbf{u}}, \mathbf{w}), \bar{\mathbf{u}}, \mathbf{w})\|_2 \\
&\leq \tau L_F L_h \|\boldsymbol{\xi}^k + \boldsymbol{\pi}_x(\mathbf{u}^k, \mathbf{w}) - \boldsymbol{\pi}_x(\bar{\mathbf{u}}, \mathbf{w})\|_2 \\
&\quad + \tau L_F L_h \|\mathbf{u}^k - \bar{\mathbf{u}}\|_2 \\
&\leq \tau L_F L_h \|\boldsymbol{\xi}^k\|_2 + \tau L_F L_h (1 + L_{\boldsymbol{\pi}_x}) \|\mathbf{u}^k - \bar{\mathbf{u}}\|_2
\end{aligned} \tag{35}$$

Substituting this into (34) and collecting terms, we finally obtain the bound

$$|\Delta V_f^1| \leq (\boldsymbol{\zeta}^k)^\top Q_1 \boldsymbol{\zeta}^k \tag{36}$$

where

$$Q_1 = \begin{bmatrix} k_1 \tau^2 + k_2 \tau & k_3 \tau^2 + k_4 \tau \\ k_3 \tau^2 + k_4 \tau & k_5 \tau^2 \end{bmatrix}$$

and where the constants k_1, \dots, k_5 can be determined from the above and are independent of τ . To bound $|\Delta V_f^2|$ we may apply (27d) to obtain

$$\begin{aligned}
|\Delta V_f^2| &\leq c_4 \|\mathbf{f}(\boldsymbol{\xi}^k + \boldsymbol{\pi}_x(\mathbf{u}^k, \mathbf{w}), \mathbf{u}^k, \mathbf{w}) - \boldsymbol{\pi}_x(\mathbf{u}^k, \mathbf{w})\|_2^2 \\
&\quad \cdot \|\mathbf{u}^{k+1} - \mathbf{u}^k\|_2 \\
&\leq c_4 L_f^2 \|\boldsymbol{\xi}^k\|_2^2 \|\mathbf{u}^{k+1} - \mathbf{u}^k\|_2,
\end{aligned}$$

where in the second line we used (33). Since 0 is an interior point of \mathcal{Z} , there exists $r > 0$ such that $\mathcal{B}_r(0) \triangleq \{\boldsymbol{\xi} \in \mathbb{R}^n \mid \|\boldsymbol{\xi}\|_2 < r\} \subset \mathcal{Z}$. For $\boldsymbol{\xi}^k \in \mathcal{B}_r(0)$ we therefore have the further bound

$$|\Delta V_f^2| \leq c_4 L_f^2 r \|\boldsymbol{\xi}^k\|_2 \|\mathbf{u}^{k+1} - \mathbf{u}^k\|_2$$

Substituting (35) into this, we finally obtain

$$|\Delta V_f^2| \leq (\boldsymbol{\zeta}^k)^\top Q_2 \boldsymbol{\zeta}^k = (\boldsymbol{\zeta}^k)^\top \begin{bmatrix} k_6 \tau & k_7 \tau \\ k_7 \tau & 0 \end{bmatrix} \boldsymbol{\zeta}^k \tag{37}$$

where k_6, k_7 are independent of τ . To bound ΔV_f^3 we apply (27b) to obtain

$$\Delta V_f^3 \leq -\rho_f \|\boldsymbol{\xi}^k\|_2^2. \tag{38}$$

Substituting the individual bounds for $|\Delta V_f^1|$, $|\Delta V_f^2|$, and ΔV_f^3 from (36), (37), and (38) back into (28), we obtain the overall bound

$$\Delta V_f \leq (\boldsymbol{\zeta}^k)^\top Q_f \boldsymbol{\zeta}^k$$

where $Q_f \triangleq Q_1 + Q_2 + Q_3$ evaluates to

$$Q_f = \begin{bmatrix} -\rho_f + k_1 \tau^2 + (k_2 + k_6) \tau & k_3 \tau^2 + (k_4 + k_7) \tau \\ k_3 \tau^2 + (k_4 + k_7) \tau & k_5 \tau^2 \end{bmatrix}.$$

Step #4 – Putting the Pieces Together: Define the composite Lyapunov candidate

$$V(\boldsymbol{\xi}, \mathbf{u}, \mathbf{w}) = V_s(\mathbf{u}) + V_f(\boldsymbol{\xi}, \mathbf{u}, \mathbf{w})$$

Along trajectories of (26), we combine the previous inequalities to compute that

$$V(\boldsymbol{\xi}^{k+1}, \mathbf{u}^{k+1}, \mathbf{w}) - V(\boldsymbol{\xi}^k, \mathbf{u}^k, \mathbf{w}) \leq (\boldsymbol{\zeta}^k)^\top Q \boldsymbol{\zeta}^k$$

where

$$Q = \begin{bmatrix} -\rho_f + (k_1 + q_1) \tau^2 + (k_2 + k_6) \tau & \star \\ k_3 \tau^2 + (k_4 + k_7 + c q_2) \tau & k_5 \tau^2 - (1 - c^2) \end{bmatrix}.$$

Note that the (1,1) block of Q is negative and is $\mathcal{O}(1)$ as $\tau \rightarrow 0$. We also have that

$$1 - c^2 = 2\tau\mu - \tau^2 L_F^2 L_\pi^2$$

and therefore the (2,2) block of Q is negative and $\mathcal{O}(\tau)$ as $\tau \rightarrow 0$. We conclude via Schur complements that there exists a $\tau^* > 0$ such that $Q < 0$ for all $\tau \in (0, \tau^*)$. Using (27a), there therefore exists $\varepsilon > 0$ such that $V(\boldsymbol{\xi}^{k+1}, \mathbf{u}^{k+1}, \mathbf{w}) - V(\boldsymbol{\xi}^k, \mathbf{u}^k, \mathbf{w}) \leq -\varepsilon V(\boldsymbol{\xi}^k, \mathbf{u}^k, \mathbf{w})$ for all $(\boldsymbol{\xi}^k, \mathbf{u}^k) \in \mathcal{B}_r(0) \times \mathcal{V}$. Standard Lyapunov arguments now complete the proof of local exponential stability.